Journal of Applied Fluid Mechanics, Vol. 19, No. 1, pp. 3254-3267, 2026. Available online at www.jafmonline.net, ISSN 1735-3572, EISSN 1735-3645. https://doi.org/10.47176/jafm.19.1.3633



Confrontation Between Smoothed Particle Hydrodynamics and Unsteady Reynolds-averaged Navier-Stokes Methods for a Sinking Rigid Body

A. Bel Hadj Taher¹, M. Ennouri^{2†}, and H. Kanfoudi²

¹ Department of Mechanical Engineering, Higher Institute of Applied Sciences and Technology of Sousse (ISSAT Sousse)
University of Sousse, Sousse, 4003, Tunisia

†Corresponding Author Email: <u>marwa.ennouri@enit.utm.tn</u>

ABSTRACT

In this article, we present detailed numerical results concerning the hydrodynamic behavior of two distinct rigid bodies; a cylinder and a wedge; interacting with a free water surface. To analyze the temporal evolution of the free surface and the resulting motion of the rigid bodies, including their vertical displacements, two numerical techniques are employed: the Weakly Compressible Smoothed Particle Hydrodynamics (WCSPH) method and the Unsteady Reynolds-Averaged Navier–Stokes (URANS) approach with the Volume of Fluid (VOF) technique. Both approaches are used to predict key physical quantities such as the vertical motion and velocity of the rigid bodies, as well as the pressure distribution within the fluid domain. The results highlight the strengths and limitations of each method, showing that WCSPH excels in capturing free surface dynamics, while URANS provides more accurate pressure predictions, using measured data for validation. The findings offer valuable insights into the appropriate method selection for marine and coastal engineering applications.

Article History

Received April 29, 2025 Revised August 13, 2025 Accepted August 17, 2025 Available online November 5, 2025

Keywords:

Reynolds-averaged Navier-stokes Smoothed particle hydrodynamics Free surface Free motion Numerical simulation Hydrodynamics

1. Introduction

Fluid-structure interaction is a common and significant physical phenomenon, particularly in engineering and environmental applications. It is often associated with highly unstable and complex events, especially within the fields of coastal, maritime, and river hydraulics. In this context, advanced numerical modeling techniques offer valuable tools to simulate and analyze such interactions, providing practical solutions to various industrial and environmental challenges.

The study of fluid-structure interaction (FSI) requires the implementation of a coupling system that links the behavior of the fluid with that of the structure. Several researchers have investigated different coupling strategies. O'Brien et al. (2000) identified three main types of coupling: (i) a one-way coupling from the structure to the fluid, (ii) a one-way coupling from the fluid to the structure, and (iii) a two-way coupling where mutual interactions are considered. Chen and Da Vitoria Lobo (1995) applied a unidirectional coupling approach to numerically simulate fluid flow carrying obstacles, using

the Navier-Stokes equations. Yuk et al. (2006) proposed a numerical model coupling the motion of a rigid object with the surrounding fluid. Greenhow and Lin (1983) conducted a fundamental study on the motion of a submerged circular cylinder. Earlier experiments by Hagiwara and Yuhara (1975), Faltinsen et al. (1977) and Campbell and Weynberg (1980) focused on the free fall of rigid cylinders onto calm water, emphasizing the balance between gravitational and hydrodynamic forces. The displacement was calculated when these forces were more significant than the weight of the rigid body.

Accurate numerical modeling of FSI remains challenging due to the complex coupling between fluid and structural domains.

In recent years, numerous digital tools have been developed to independently model structural behavior and fluid flows. However, a major limitation of these tools lies in their lack of integrated coupling, which restricts their effectiveness in accurately resolving fluid-structure interaction (FSI) phenomena. Typically, the FSI process is divided into two sequential stages. The fluid equations are solved on the structure's surface in the first stage. The

² Hydraulic and Environmental Modeling Laboratory, Department of Civil Engineering, National Engineering School of Tunis (ENIT), University of Tunis El Manar, Tunis, 1002, Tunisia

Nomenclature				
A	variable	P_k	production of turbulence	
ALE	Arbitrary Lagrangian-Eulerian	r	specific point	
В	compressibility coefficients	RANS	Reynolds-Averaged Navier-Stokes	
C_{θ}	sound speed	SPH	Smoothed Particle Hydrodynamics	
C_{μ}	a dimensionless constant	U_i	average velocity	
DEM	Discrete Element Method	$-u_iu_i$	Reynolds stresses	
DOF	Degree Of Freedom	VOF	Volume of Fluid	
F	forces applied on the solid	W	kernel function	
F_i	source term for the momentum			
FSI	Fluid-Structure Interaction	δ_{ij}	Kronecker delta	
g_i	acceleration of gravity	ε	dissipation rate of turbulent energy	
h	smoothing length	ν	kinematic viscosity	
k	turbulent kinetic energy	ν_t	eddy viscosity	
m	mass of the rigid solid	$\overset{\circ}{ ho}$	density of the fluid	
P	pressure	$ au_{j}$	viscous stresses	
P_{θ}	reference pressure	Π_{ab}	artificial viscous pressure	

resulting pressure, stress, or force fields are then transferred to a structural solver, which computes the corresponding displacements and deformations of the structure.

To model and track fluid flows, two primary numerical approaches are commonly employed: the Eulerian and Lagrangian methods. The Eulerian approach, which relies on a fixed computational mesh, is well-suited for simulating fluid flows ranging from single-phase to multiphase systems. It offers the advantage of facilitating mass conservation and is generally straightforward to implement. In contrast, the Lagrangian approach focuses on tracking individual fluid particles as they move through space. Its key advantage lies in being mesh-free, making it particularly effective for problems involving large deformations or significant displacements of rigid bodies within the fluid domain.

According to the literature, Reynolds-Averaged Navier-Stokes (RANS) methods have been widely employed to investigate various fluid mechanics phenomena, particularly wave dynamics in coastal regions. For turbulence modeling, the standard k- ε closure model has frequently been used due to its robustness and simplicity. To capture the motion of the free surface, the RANS approach is typically coupled with the Volume of Fluid (VOF) method. This combination has proven effective in simulating complex free surface flows and has been adopted in several studies, including those by Chang et al. (2001), Liu and Al-Banaa (2004), and Chang et al. (2005).

The study conducted by Takahashi et al. (2003) explores and discusses the impact of a solid object on a liquid surface. However, their numerical model neglects the influence of hydrodynamic forces acting on the object itself. In response to this limitation, Singh et al. (2003) proposed an improved numerical approach based on the Arbitrary Lagrangian-Eulerian (ALE) method, originally introduced by Hirt et al. (1974), and later refined for fluid-structure interaction problems, provides a compromise between Eulerian and Lagrangian frameworks. This method utilized two separate solvers, one for computing

the fluid flow around obstacles and another for determining the displacement and deformation of the structures. A major drawback of this technique was the need for frequent remeshing as the object moved, which often led to difficulties in maintaining mesh quality and, in some cases, caused the system solver to fail. To address such limitations, Belytschko et al. (2014) developed a mixed Lagrangian-Eulerian formulation specifically designed to improve the modeling of fluid-structure interaction problems.

As an alternative to overcome the challenges associated with coupling techniques, Müller et al. (2003) developed the Smoothed Particle Hydrodynamics (SPH) method to simulate fluid-object interactions. This meshfree approach has since been adopted and further extended in subsequent studies, including those by Losasso et al. (2008) and Fang et al. (2009), for modeling complex fluid-structure interactions.

Several studies have investigated the relative strengths of mesh-based and mesh-free methods for modeling fluid-structure interactions and free-surface impacts. The study by Turhan et al. (2019) compared SPH and RANS (solved via Flow-3D) for dam-break flows involving density-varying fluids (salt water). Both methods accurately captured initial wave propagation, with close agreement to experimental data in early stages. However, the results highlight SPH's utility for mesh-free simulations of complex flows but underscore RANS's robustness for scenarios requiring precise turbulence modeling. The authors recommend further SPH parameter optimization (e.g., viscosity coefficients) to enhance accuracy. Neves et al. (2016) performed a direct comparison of RANS (OpenFOAM) and SPH (DualSPHysics) for wave breaking and found that while RANS predicted free-surface elevation more accurately, SPH better captured velocity fields during breaking. Brizzolara et al. (2009) and Hosain et al. (2018) have applied both SPH and RANS/VOF to sloshing problems. While SPH captured free-surface motion effectively, it showed pressure fluctuations unless carefully tuned. RANS/VOF produced more stable pressure fields but at higher computational cost. Similarly, Sasson et al. (2016) compared mesh-based RANS and WCSPH methods in slamming problems, noting that RANS method slightly better predicts the acceleration values prior to peak acceleration, while the quick setup of SPH simulations, together with the use of GPU accelerated computing, gives advantages. Finally, Tafuni et al. (2022) reviewed recent SPH applications in fluid–structure interaction, emphasizing advancements and juxtaposing SPH with mesh-based

Despite these efforts, and while both SPH and RANS methods have been widely used for water entry problems, comprehensive evaluations involving varied rigid body geometries using both approaches remain limited. Most prior studies focus on a single geometry typically wedges and apply either SPH or RANS independently. Few works directly compare the performance of both methods under identical initial and boundary conditions, particularly across geometries that induce different flow responses. This study addresses that gap by examining both cylindrical and wedge-shaped body entries using weakly compressible SPH (WCSPH) and RANS approaches, offering a broader and more balanced assessment of their capabilities

In this study, the RANS and SPH numerical models are applied to address the problem of free surface flow and the penetration of two rigid bodies into water. The first is a cylindrical solid undergoing free fall, while the second is a triangular-shaped body introduced into the water with an initial horizontal velocity at the moment of contact. These geometries were selected due to their relevance in naval and coastal engineering applications, cylinders model offshore pile structures, while wedges simulate ship bow or breakwater impacts.

The main objective is to evaluate the strengths and limitations of each method by comparing their numerical predictions with experimental data available in literature. It contributes to the literature by offering a detailed, sideby-side numerical comparison between WCSPH and Unsteady RANS (URANS) methods for modeling two geometrically distinct rigid bodies, highlighting methodological trade-offs and validating results with experimental data. The first part of the paper introduces the RANS and SPH models along with their respective mathematical formulations. The second part presents a detailed analysis of the simulation results, followed by a discussion comparing the performance and accuracy of both approaches. Our goal is to provide practical guidance on method selection for real-world applications.

2. METHODOLOGY AND EQUATIONS

In this section, we present the mathematical formulations underlying the two numerical models RANS and SPH following the approaches proposed by Panizzo (2004a, 2004b); Panizzo and Dalrymple (2004) and Yuk et al. (2006).

The SPH simulations were conducted using an opensource code DualSPHysics developed in C + + language, based on the formulation described in (Crespo et al., 2011) and recently in (Crespo et al., 2015). The SPHysics code has been applied and validated across a range of scenarios (Dominguez et al., 2022), including wave breaking phenomena (Dalrymple & Rogers, 2006), dam-break events (Crespo et al., 2008; Gomez-Gesteira, 2010), and interactions with both fixed coastal structures (Gomez-Gesteira et al., 2004) and mobile breakwaters (Rogers et al., 2010). Additionally, a shallow water adaptation of the code has been developed and tested (Vacondio et al., 2012, 2013). Conversely, the RANS simulations were carried out using Ansys-CFX in conjunction with volume of fluid (VOF) scheme. They are widely validated for rigid body water-impact problems, capturing free-surface dynamics, pressure spikes, drag, and fluid-structure interaction with dynamic mesh and turbulence modelling Elangovan, 2008; Mahmoodi et al., 2018; Singh & Pal, 2023).

2.1 RANS Model

In flow modeling, using unsteady 2D RANS equations, water and air are considered as a single homogeneously mixed fluid, whose equation is:

$$\frac{\partial U_i}{\partial x_i} = 0 \tag{1}$$

$$\frac{\partial U_i}{\partial t} + \frac{\partial (U_j U_i)}{\partial x_j} = \frac{-1}{\rho} \frac{\partial P}{\partial x_i} + \frac{\partial}{\partial x_j} \left[\nu \left(\frac{\partial U_i}{\partial x_j} + \frac{\partial U_j}{\partial x_i} \right) - \overline{u_i u_j} \right] + g_i + F_i$$
(2)

where the average velocity and pressure are given by U_i and P, the acceleration of gravity and the kinematic viscosity are respectively represented by g_i and ν , the density of the fluid is given by ρ , and F_i is the source term for the momentum. These equations include new terms, called Reynolds stresses $-u_iu_j$, which reflect the production of velocity fluctuations and constitute the transfer of convective motion due to velocity fluctuations. They pose a problem of closing the governing equations. Therefore, the turbulence models make it possible to provide phenomenological laws to close the problem. The first-order closure is based on turbulent viscosity, and it is considered the best way to approximate the Reynolds tensor.

The Reynolds stress is given by Eq. (3):

$$-\overline{u_i u_j} = \nu_t \left(\frac{\partial U_i}{\partial x_j} + \frac{\partial U_j}{\partial x_i} \right) - \frac{2}{3} k \delta_{ij}$$
 (3)

where the Kronecker delta is given by δ_{ij} , the turbulent kinetic energy is represented by k.

$$k = \frac{\overline{u_l^2}}{2} \tag{4}$$

and the eddy viscosity is given by:

$$v_t = C_\mu \frac{k^2}{\varepsilon} \tag{5}$$

where C_{μ} is a dimensionless constant. Two-equation models are widely used. The turbulent length scale is defined from the turbulent kinetic energy and the dissipation rate. They are determined by their transport equations.

The transport equations of k and ε are given by Eqs (6) and (7):

A. Bel Hadj Taher et al. / JAFM, Vol. 19, No. 1, pp. 3254-3267, 2026.

$$\frac{\partial k}{\partial t} + \frac{\partial (U_j k)}{\partial x_i} = \frac{\partial}{\partial x_i} \left[\left(\nu + \frac{\nu_t}{\sigma_k} \right) \frac{\partial k}{\partial x_i} \right] + P_k - \varepsilon \tag{6}$$

$$\frac{\partial \varepsilon}{\partial t} + \frac{\partial (U_j \varepsilon)}{\partial x_i} = \frac{\partial}{\partial x_i} \left[\left(v + \frac{v_t}{\sigma_{\varepsilon}} \right) \frac{\partial \varepsilon}{\partial x_i} \right]$$

$$+\frac{\varepsilon}{k}(C_{\varepsilon 1}P_k - C_{\varepsilon 2}\varepsilon) \tag{7}$$

Where P_k denotes the production of turbulence:

$$P_k = \nu_t \left(\frac{\partial U_i}{\partial x_j} + \frac{\partial U_j}{\partial x_i} \right) \frac{\partial U_j}{\partial x_j} \tag{8}$$

The values of these constants $C_{\mu} = 0.09$, $C_{\varepsilon I} = 1.44$, $C_{\varepsilon 2} = 1.92$ and of the turbulent Schmidt numbers $\sigma_{k} = 1$ and $\sigma_{\varepsilon} = 1.3$ are used in the present computations.

VOF-Based Free Surface Tracking in URANS

Based on Landau and Lifshitz (2014), the free surface can be evaluated as a tangential discontinuity, and the surface speed shows continuity in the normal and tangential directions. On the other hand, there is discontinuity in the normal direction between two domains of different densities.

By adopting the VOF method, continuous free surfaces can be controlled and tracked using a scalar variable, where a zero value indicates an empty area or volume. On the other hand, a unit value suggests a small area, or a small volume occupied by the fluid. Thus, a fractional value of *F* between 0 and 1 in a discrete mesh represents a segment of the interfacial region of two fluids:

$$F(\vec{x},t) = \begin{cases} 1 & \text{In fluid} \\ [0 < F < 1] & \text{At the free surface} \\ 0 & \text{In the void} \end{cases}$$
 (9)

For incompressible flows, $F(\vec{x},t)$ is given by the following expression (Hirt et al., 1974):

$$F\left(\vec{x},t\right) = \frac{\rho(\vec{x},t)}{\rho_f} \tag{10}$$

with:

$$\frac{\partial F}{\partial t} + \frac{\partial (F \ U_i)}{\partial x_i} = 0 \tag{11}$$

Governing Equations for Rigid Body Translation

The displacement of the object in a fluid is modeled by its movement equations. In our study, we assume that a displacement is a translation along the \underline{Y} axis (one-Degree-Of-Freedom (DOF) method). This choice is related to experimental measurements available for the confrontation of the proposed numerical model.

The balance of forces on a rigid body is given by Eq. (12):

$$mx = F \tag{12}$$

where m and F respectively denote the mass of the rigid solid and the forces applied on the solid (see Fig. 1).

$$F = F_{flow} + mg + F_{Ext} (13)$$

where the force exerted by the water, the force of gravity and the external forces are given respectively by F_{flow} , mg

and F_{ext} . The force applied by the fluid (water) is given by Eq. (14):

$$F_{flow} = \sum_{j=1}^{n} \left(-p_j n_j + \tau_j \right) s_j \tag{14}$$

where the pressure applied to the surface S_j of the normal vector n_j of a control volume is given by p_j , and where τ_j represents the viscous stresses:

2.2 Weakly Compressible SPH Model for Free Surface Flows

The Smoothed Particle Hydrodynamics (SPH) method was originally developed by Gingold and Monaghan (1977) and Lucy (1977) for the simulation of astrophysical phenomena. It was later extended by Monaghan (1994) to address problems involving free surface flows and fluid-structure interactions.

Mathematical formulation of fluid method

The transformation of fluid equations into integral form is carried out using a kernel function W, which has a radius of 2h. This kernel serves as a weighting function that defines a physical variable A at a specific point r. The estimate of the kernel for variable A is given by the following expression (Morris, 1996).

$$A(r) = \int_{space} A(r')W(r - r', h)dr'$$
 (15)

The spatial discretization is defined by the smoothing length h. The *W* function has several properties, such as:

$$\int_{space} W(r - r', h) dr' = 1 \tag{16}$$

$$\lim_{h \to 0} W(r - r', h) = \delta(r - r') \tag{17}$$

The gradient of function A is given by the following expression (Morris, 1996):

$$\nabla_r A(r) = \int_{snace} A(r') \nabla_r W(r - r', h) dr'$$
 (18)

In SPH, the determination of physical variables is carried out at each individual particle. From Eqs. (15) and (18), the physical variable A and its gradient can be expressed as a summation over the neighboring particles b of particle a, as follows:

$$A_a = \sum_{h=1}^N V_h A_h W_{ah}$$
 and

$$\nabla_a A_a = \sum_{b=1}^N V_b A_b \nabla_a W_{ab} \tag{19}$$

where $W_{ab} = W(r_a - r_b, h)$ and

$$V_i = \frac{m_i}{\rho_i} \tag{20}$$

Hence the gradient of \underline{A} is given by:

$$\nabla_{a} A_{a} = \frac{1}{2} \sum_{b=1}^{N} m_{b} (A_{b} - A_{a}) \nabla_{a} W_{ab}$$
 (21)

Thus, the continuity and momentum equations can be reformulated in the following form:

$$\frac{d\rho_a}{dt} = \sum_{b=1}^{N} m_b (v_a - v_b) \nabla_a W_{ab}$$
 (22)

$$\frac{dv_a}{dt} = -\sum_{b=1}^{N} m_b \left(\frac{P_b}{\rho_b^2} - \frac{P_a}{\rho_a^2} \right) \nabla_a W_{ab}$$
 (23)

We consider the fluid to be real. We rewrite Eq. (23) as follows:

$$\frac{dv_a}{dt} = -\sum\nolimits_{b=1}^{N} m_b \left(\frac{P_b}{\rho_b^2} - \frac{P_a}{\rho_a^2} + \prod_{ab} \right) \nabla_a W_{ab} \tag{24}$$

where \prod_{ab} denotes the artificial viscous pressure, and it is given by Eq. (25):

$$\Pi_{ij} = \begin{cases}
\frac{-\alpha C_{ab} \mu_{ab} + \beta \mu_{ab}^2}{\rho_{ab}} & \text{if } v_{ab} \cdot r_{ab} < 0 \\
0 & \text{otherwise}
\end{cases}$$
with $\mu_{ab} = hv_{ab} r_{ab} (r^2 + r^2)$:

where C_a and C_b are the speed of sound for particles a and b; h is the smoothing length, $\alpha = 0.01$, and $\beta = 0$ are two constants for general hydraulic problems.

We adopt the kernel function developed by Johnson et al. (1996). This function is very suitable for studying the interaction of the object with the free surface. It is given by the following expression:

$$s = r/h \in [0.0; 2.0]$$
as:

$$W(r,h) = \frac{1}{\pi h^2} \left(\frac{3}{8} s^2 - \frac{3}{2} s + \frac{3}{2} \right)$$
 (26)

$$W'(r,h) = \frac{1}{\pi h^3} \left(\frac{3}{4} s - \frac{3}{2} \right) \tag{27}$$

We calculate the pressure of the fluid based on the equation of state, which takes into account the compressibility of the fluid (Batchelor, 2000).

$$P = P_0 + B \left[\left(\frac{\rho}{\rho_0} \right)^{\gamma} - 1 \right] \tag{28}$$

where P_0 represents the reference pressure, $\gamma = 7$ and B represents the compressibility coefficients.

$$B = \frac{C_0^2 \rho_0}{\gamma} \tag{29}$$

where ρ_{θ} denotes the reference density, and C_{θ} is the sound speed.

Motion of Rigid Body

To track and evaluate rigid body motions, which are categorized into translational and rotational movements, the SPH model utilizes the Discrete Element Method (DEM), originally developed by Cundall and Strack (1979). The two types of motion are illustrated in Fig. 1.

Newton's equations allow for the calculation of rotational motion.

$$M_I \frac{dV_I}{dt} = \sum_{k \in I} m_k f_k \tag{30}$$

$$I_{\frac{\mathrm{d}\Omega}{\mathrm{d}t}} = \sum_{k \in I} m_k (r_k - R_I) f_k \tag{31}$$

where M_I , V_I , I_I , Ω_I , and R_I respectively represent the mass, the speed, the inertia tensor, the angular speed and the center of gravity of object I, and where f_k represents the mass force applied to particle k.

The main numerical parameters adopted for the SPH simulations are summarized in Table 1. These values were selected based on recommended practices for free-surface

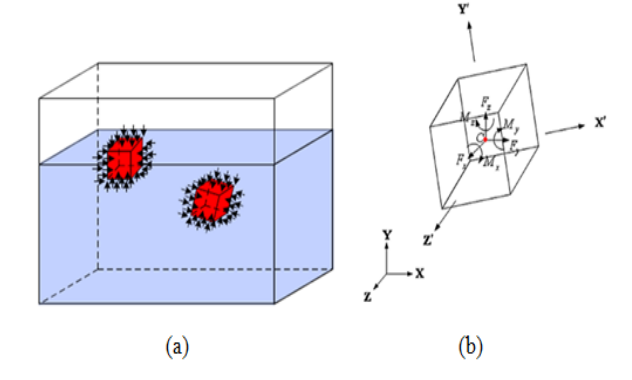


Fig. 1 (a) Movement of rigid body in liquid, where the arrows represent the pressure of the fluid acting on the faces of the solid. (b) Rotation of rigid body along x, y, z axes

Table 1 Key SPH simulation parameters

Parameter	Value	Parameter	Value
Δp	0.004 m	γ	7
Tank size	2.0 × 0.5 m (L×H)	coesound	20
Interaction kernel	Johnson et al. (1996)	speedsound	auto
coefh	1.2	cflnumber	0.2
ρ_0	1000 kg/m ³	α	0.01

impact problems and are consistent with parameter ranges reported in previous DualSPHysics studies (Altomare et al., 2015; Crespo et al., 2011, 2015; Dominguez et al., 2022) ensuring both numerical stability and physical accuracy.

With this parameter setup, the SPH model is expected to accurately capture the free-surface dynamics and rigid body motions under study, providing a consistent basis for comparison with the RANS/VOF simulations presented in the following section.

3. RESULTS AND DISCUSSION

To evaluate the predictive capabilities of the previously presented RANS and SPH approaches, two different rigid bodies are considered in their interaction with a free water surface. The first body is a cylinder with two distinct densities, while the second is a wedge. The computational domain for the first solid is illustrated in Fig. 2. For both numerical approaches, it is assumed that the rigid body is in free fall, perfectly vertical, and does not undergo any rotation during its motion. In the RANS approach, free-slip boundary conditions are applied at all surfaces. In the SPH model, the computational domain is confined to a height of 2.0 m and a width of 0.5 m, with a particle diameter of 0.004 m. Particles are spaced 0.004 m apart throughout the domain.

For both RANS and SPH methods, convergence was tested by halving the mesh size and particle spacing, respectively, and verifying that the resulting penetration depth and velocity predictions differed by less than 5%.

Further refinement showed no significant change, confirming numerical convergence

3.1 Water Entry of Cylinder

The numerical results for the free fall of rigid bodies in stable water are compared with the experimental data presented by Greenhow and Lin (1983). Two different models are tested in their experiments: a neutral buoyancy cylinder and a semi-floating cylinder. The term "neutral buoyancy" refers to the condition where the object's weight is exactly balanced by the buoyant force, while "half buoyancy" indicates that the object's weight is half of the buoyant force acting on a fully submerged body. An explanatory diagram of the experimental setup is shown in Fig. 2. The distance between the rigid body, with a diameter of 0.11 m, and the free water surface is 0.5 m. The initial velocity of the rigid body at the water surface is determined using the equation $V_0 = (2gh)^{1/2} = 2.955$ m/s. Therefore, the time required for the body to reach the water surface is calculated as $t_0 = V_0/g = 0.301$ s.

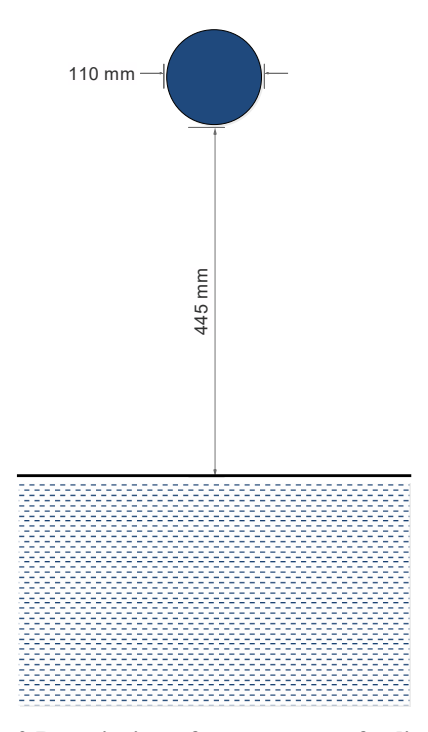


Fig. 2 Description of water entry of cylinder

Case I: d=0.5

We consider that the density of water is $1000~kg~/m^3$, the kinematic viscosity is $10^{-6}~m^2/s$, and the surface tension is 0.0736~N/m. An explanatory diagram of the problem as well as the initial pressure contour are presented in Fig. 3. The water is initially stable, and the variation of pressure is due to the hydrostatic pressure.

The time evolution of the cylinder's penetration into the water, as predicted by both numerical approaches, is shown in Fig. 4. The results indicate that the RANS approach yields a slightly greater penetration depth compared to the SPH method. However, both numerical models demonstrate good agreement with the experimental measurements, confirming the reliability of

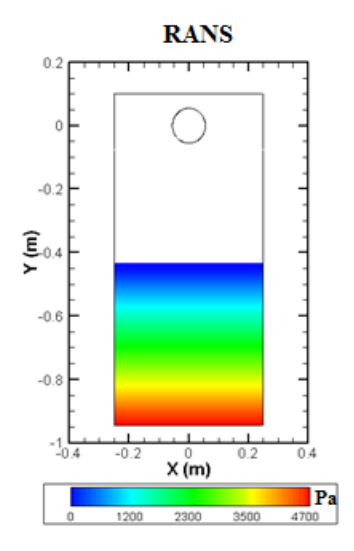


Fig. 3 Initial conditions of cylinder considered for simulation for RANS approach

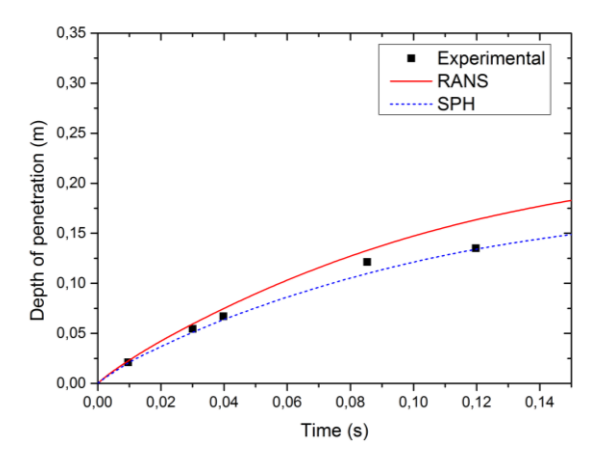


Fig. 4 Comparison between calculated and measured cylinder penetration depths: SPH (blue line), RANS (red line) results, and experimental measurements (black square dots (Greenhow & Lin, 1983))

the simulations for modeling the fluid-structure interaction during the cylinder's descent.

The time evolution of the cylinder's velocity is illustrated in Fig. 5. It is observed that the cylinder's speed initially decreases before reaching the water surface. During this phase, the velocity drops from an initial value of 0.95 m/s to 0.5 m/s at t=0.3. Upon contact with the water surface, the speed continues to decrease, reaching a minimum of 0.35 m/s at t=0.45s. After this point, the velocity begins to increase again, reaching 0.4 m/s by t=0.8 s. Throughout the simulation, both the RANS and SPH approaches follow similar trends. Between t₀ and the moment of water entry (t=0.301 s), the two models exhibit nearly identical behavior. However, after this point, the SPH curve begins to diverge, ultimately returning to a value of 0.52 m/s by the end of the simulation. The speed evolution can be divided into two distinct phases. The first phase, referred to as the descent phase, is characterized by deceleration. The second phase, beginning at t=0.5 s, corresponds to the rigid body's upward movement, which explains the observed increase in speed. At the free

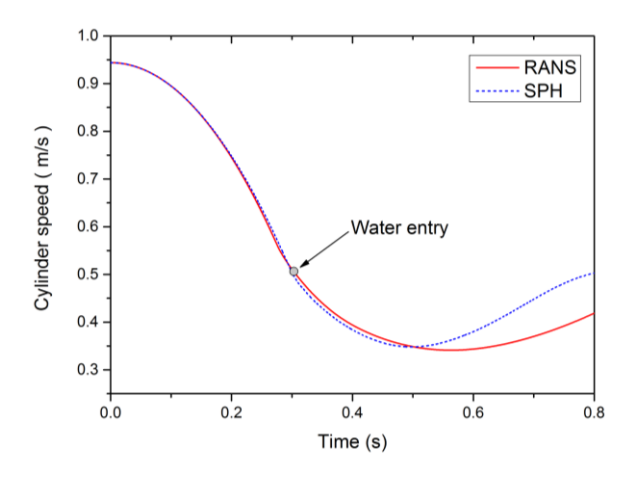


Fig. 5 Velocity field computed by RANS and SPH models

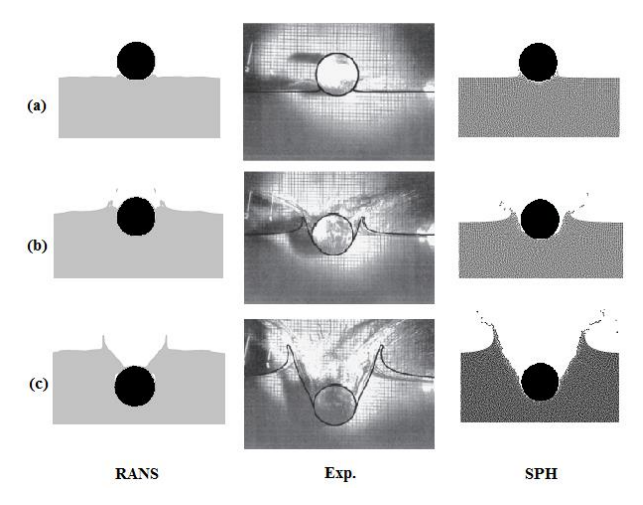


Fig. 6 Comparison between digital and experimental free surface profiles for a semi-floating cylinder at three times (a) t = 0.005 s, (b) t = 0.033 s and (c) t = 0.085 s. On the right (SPH method), on the left (RANS method), and in the center (experimental photos according to Greenhow and Lin (1983))

surface, the SPH model reaches a speed of 0.52 m/s, while the RANS model reaches 0.45 m/s. It is evident that, during this upward phase, the RANS model provides more accurate results, as the final velocity calculated by the RANS approach is closer to the expected value at water entry.

Figure 6 presents a comparison between the free surface state and the positions of the cylinders, as calculated and measured, at t=0.005 s, t=0.033 s, and t=0.085 s. The free surface of the fluid (water) is considered as the temporal origin of the simulation. Once the rigid body is submerged, ripples and fragmentation begin to appear on the free surface, promoting the separation of the flow and the formation of a jet around the cylinder. This jet intensifies progressively as the simulation time increases. Both the RANS and SPH methods capture the overall dynamics of the phenomenon; however, the SPH model better predicts the shape of the water surface, the formation of nearly vertical jets, and the height of the resulting water column. This is primarily due

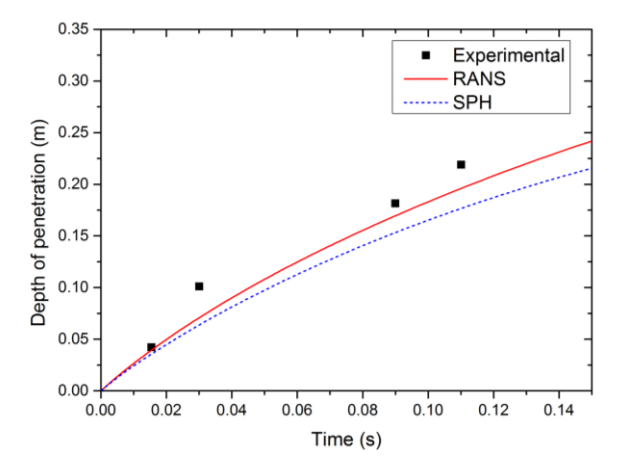


Fig. 7 Comparison between calculated and measured cylinder penetration depths: SPH (blue line), RANS (red line) results, and experimental measurements (black square dots, (Greenhow & Lin, 1983))

to the reflective nature of the SPH method, which minimizes particle clumping through its disorderly scattering of particles and the artificial stress in the core function, leading to a more accurate representation of the free surface dynamics.

Case II: d=1

After testing both approaches with a half-buoyancy cylinder, this section explores the case of a cylinder with neutral buoyancy.

Figure 7 presents a comparison between the temporal variations in the cylinder's penetration depth into the water, as calculated using both the SPH and RANS approaches, along with the corresponding experimental measurements. It is observed that the measured values are slightly higher than the calculated ones. In this case, the RANS approach provides results that are closer to the measured penetration depth, as compared to the SPH method, which shows a slight deviation. This suggests that the RANS model better captures the dynamics of the neutral buoyancy cylinder's interaction with the water surface in this specific scenario

Figure 8 illustrates the velocity of the neutrally buoyant cylinder, as obtained from both the RANS and SPH models. Three distinct phases can be observed in the velocity evolution. The first phase is an acceleration phase, where the cylinder moves vertically from the top to the water surface, with the velocity increasing from an initial value of 0 m/s. This is followed by a deceleration phase, during which the cylinder moves from the water surface downward, losing speed. Finally, the imbalance between the cylinder's gravity and the buoyant force causes the body to rise back to the free surface, marking the onset of the third phase. In this phase, a certain stability in the velocity becomes evident. Both the RANS and SPH models capture these phases, albeit with a phase shift, and the RANS curve exceeds the SPH curve in terms of velocity

The numerically predicted free surfaces, shown in Fig. 9, align well with the actual states of the free surface. The penetration process is both deeper and faster due to

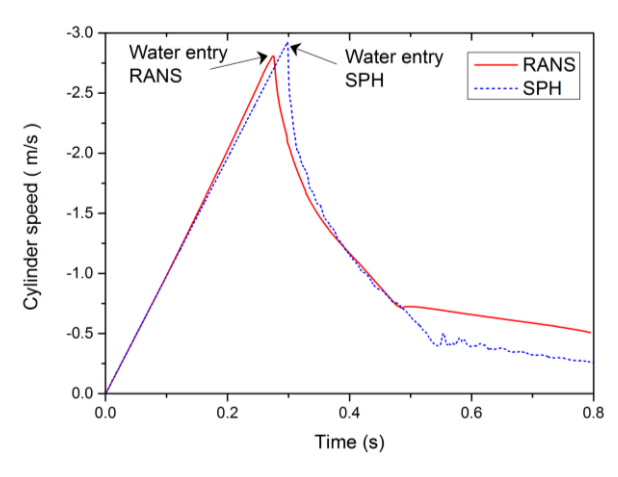


Fig. 8 Velocity field computed by RANS and SPH models

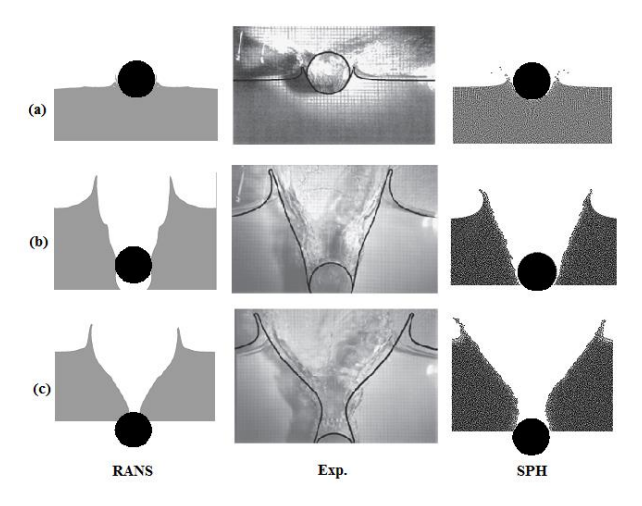


Fig. 9 Comparison between digital and experimental free surface profiles for semi-floating cylinder at three times (a) t = 0.015 s, (b) t = 0.11 s and (c) t = 0.2 s. On the right (SPH method), on the left (RANS method), and in the center (Experimental photos according to Greenhow and Lin (1983))

the increased gravitational effect. As the cylinder's weight increases, the free surface condition becomes more pronounced, and the size of the jet intensifies. The results indicate that the SPH model closely matches the experimental measurements. Further analysis reveals that the SPH model provides more accurate predictions of the interaction between the rigid body and the free surface compared to the RANS method.

One key reason for this improved performance is the nature of the SPH approach, which uses a particle-based method to simulate fluid flow. This allows the SPH model to more accurately capture complex fluid behaviors such as free surface deformations, jet formation, and particle interactions. In contrast, the RANS method, which relies on averaged flow equations, tends to smooth out these fine-scale dynamics, potentially leading to less accurate predictions in cases involving sharp changes in fluid velocity or pressure, such as during the impact and interaction with a rigid body. Additionally, the SPH model's "meshless" nature helps in handling large displacements and complex interactions without the issues

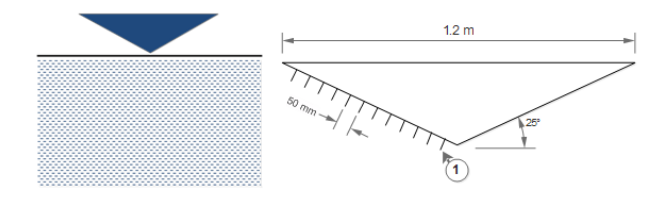


Fig. 10 Description of study domain and wedge details

of mesh distortion or remeshing, which can occur in traditional grid-based methods like RANS. As a result, the SPH model is better suited to capture the detailed, localized effects of the rigid body's motion on the fluid, leading to a more faithful representation of the free surface dynamics.

3.2 Water Entry of Wedge

This section presents the study of the interaction between a wedge in free fall and the free surface of water. The investigation involves immersing a wedge with a mass of 94 kg, a lifting angle of 25°, and a square upper section measuring 1.2 x 1.2 m, into a free water surface at a speed of 5 m/s, as shown in Fig. 10.

As in the previous two cases, the objective of this study is to compare the results from both the SPH and RANS approaches with the experimental measurements reported by Yettou et al. (2006).

In this section, we present the temporal distribution of pressure on one side of the wedge (2D), as calculated by both models. The pressure is measured using 12 transducers spaced 50 mm apart, as shown in Fig. 10.

At t = 0 s and before the bilge penetrates the water, the water pressure increases as a function of the depth. Thus, the hydrostatic pressure is given by the following expression.

$$P = \rho. g. h = 9670 Pa$$

The pressure results found by the numerical simulation for the SPH and RANS methods are illustrated in Fig. 11.

The displacement of the wedge as a function of time is calculated using both the SPH and RANS numerical approaches. A comparison between the numerical results and the experimental measurements is presented in Fig. 12.

Between t = 0s and t = 0.8s, there is a good agreement between the different results in terms of both phase and amplitude. However, from t = 0.8s onwards, a displacement offset is observed, with the SPH approach diverging from both the RANS results and the experimental measurements. At t = 0.4s, an imbalance between the gravity of the wedge and the buoyancy of the fluid causes the rigid body to move back towards the free surface, which is reached at t = 0.8s. Once the solid reaches the free surface, waves begin to form due to the separation between the fluid and air domains. It is also noticeable that the RANS method is better able to track the solid's movement at the free surface level compared to the SPH method. Additionally, it is observed that the simulated displacement of the rigid body does not reach the bottom of the channel.

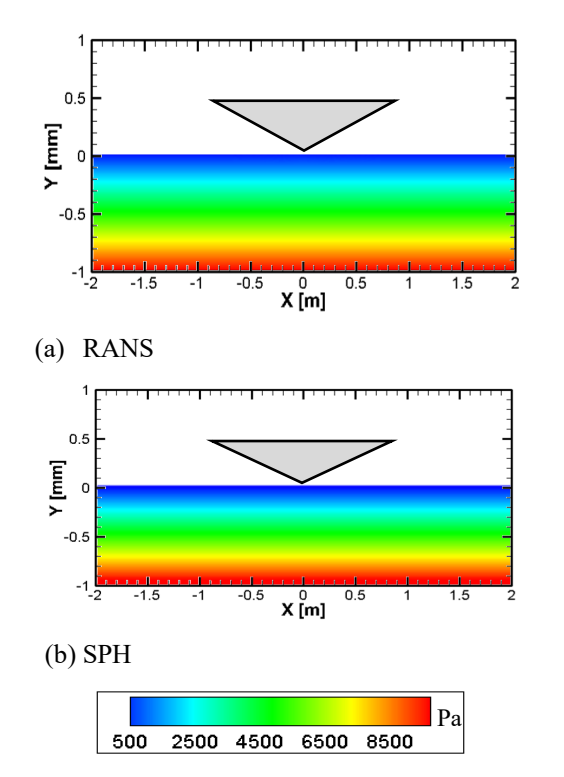


Fig. 11 Distribution of pressure field calculated at t = 0s by two approaches RANS (a); SPH (b)

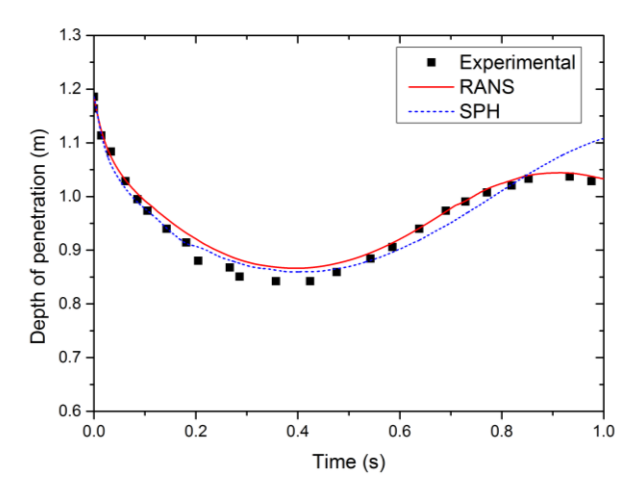


Fig. 12 Confrontation between calculated and measured values of wedge penetration depths: SPH approach (blue line), RANS approach (red line), and experimental measurements (black square points (Yettou et al., 2006))

Figure 13 presents the temporal evolution of the wedge speed for both the SPH and RANS numerical approaches. These results are compared with the experimental measurements. The speed cycle is defined by three phases:

First phase: During the vertical movement from top to bottom, the wedge's speed decreases from an initial value of $V_0 = 5$ m/s to zero at t = 0.4s. This is the deceleration phase, which can be further divided into two sub-phases. In the first sub-phase, the speed decreases linearly from 5 m/s to 2 m/s over 0.01s, corresponding to a deceleration of 300 m/s². The simulation results show a

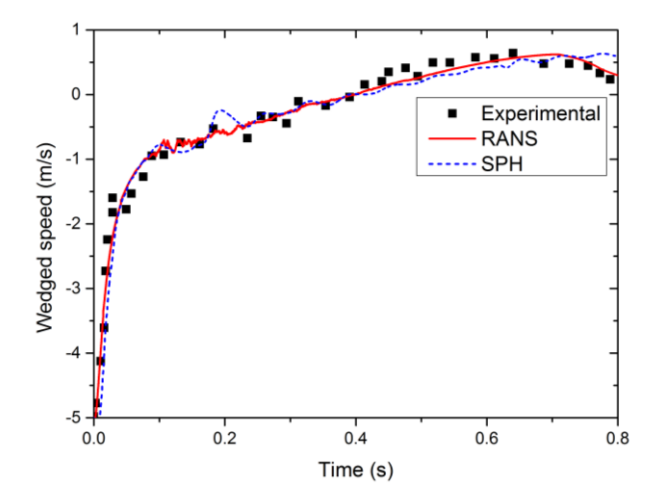


Fig. 13 Confrontation between calculated and measured values of the temporal evolution of speed of the wedge

good agreement with the experimental data during this phase.

In the second sub-phase, the speed drops from 2 m/s to 0 m/s over a time interval of 0.35s, corresponding to a deceleration of 5.71 m/s². In the SPH simulated speed signal, oscillations are observed, which are attributed to pressure waves in the field reflecting at the bottom.

Second phase: At t = 0.4s, the solid begins moving from bottom to top with an initial speed of 0 m/s, reaching a speed of 0.5 m/s at the surface.

Third phase: This phase is characterized by a further reduction in speed, and it is evident that the RANS method produces more reliable results than the SPH method in this context.

Figure 14 presents the pressure oscillations calculated and measured at the different transducers. Transducer 1, which is the first to encounter the water, displays a maximum pressure value at t = 0.005s. At this moment, all other transducers show zero values, as they are not submerged. This explains the phase shift between the maximum values recorded by each transducer during the wedge's penetration process. For instance, for transducer number 5, the maximum pressure occurs at t = 0.017s.

From the data in Fig. 14, it can be seen that the pressures calculated by the RANS approach closely match the measured pressures, in contrast to the SPH approach, which shows a significant deviation. This discrepancy is attributed to the empirical pressure model used by the SPH method.

The high-frequency pressure oscillations observed in the WCSPH simulation in Fig. 14 are a known limitation of standard SPH formulations. Recent advances such as the δ -SPH method (Antuono et al., 2010) offer improved pressure stability through density diffusion terms and could be considered for future improvements.

Figure 15 illustrates the pressure field distributions calculated by both methods around the wedge at t = 0.045s. High pressures, approximately 24 kPa, are observed beneath the wedge. These high-pressure zones

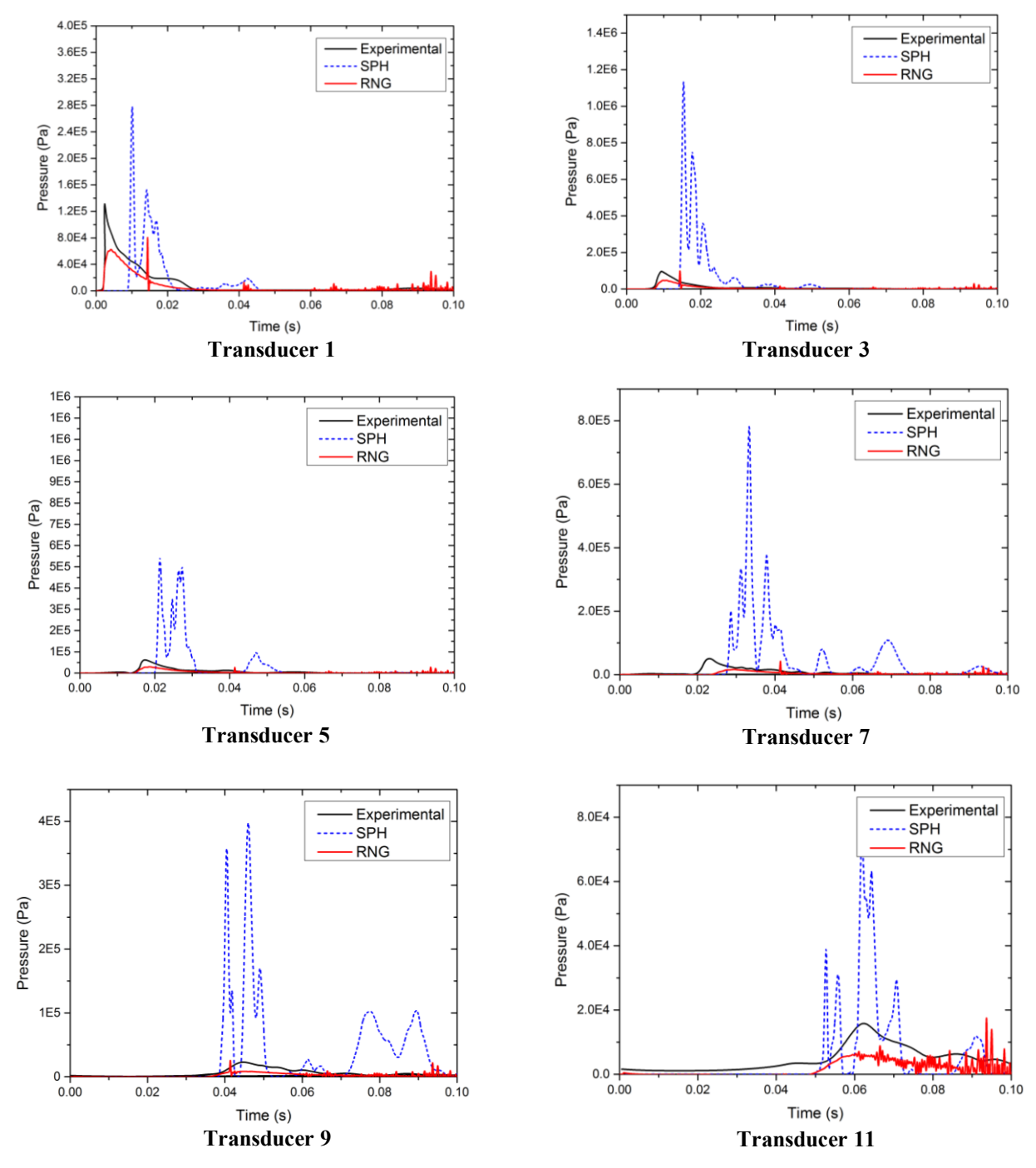


Fig. 14 Experimental data and numerical results RANS model; SPH model for time histories of pressure for six transducers

diffuse laterally as the water beneath the wedge is displaced, a behavior captured by both numerical approaches. It is also noted that the RANS method produces a symmetrical pressure field relative to the wedge's vertical axis, while the SPH method results in asymmetrical pressure waves moving through the field. The pressure calculation is considered one of the limitations of the SPH method. Pressure discrepancies are due to SPH's dependence on an empirical equation of state and its poor resolution near solid boundaries.

Figure 16 illustrates the water velocity vectors calculated by both the RANS and SPH methods at t = 0.045s. When the wedge is immersed in water, the fluid is

displaced to both sides of the solid, generating water jets. One of the limitations of the SPH method is its modeling of velocity at the free surface. This is evident from the velocity vectors, which appear to exit the fluid domain, highlighting the method's difficulty in accurately capturing the behavior at the free surface.

The differences observed between WCSPH and RANS/VOF results particularly in pressure, velocity, and streamlines stem from their distinct numerical frameworks. WCSPH, being mesh-free, better captures the violent free-surface breakup during wedge entry but shows more pressure noise, especially near impact zones. RANS/VOF, with its mesh-based formulation and

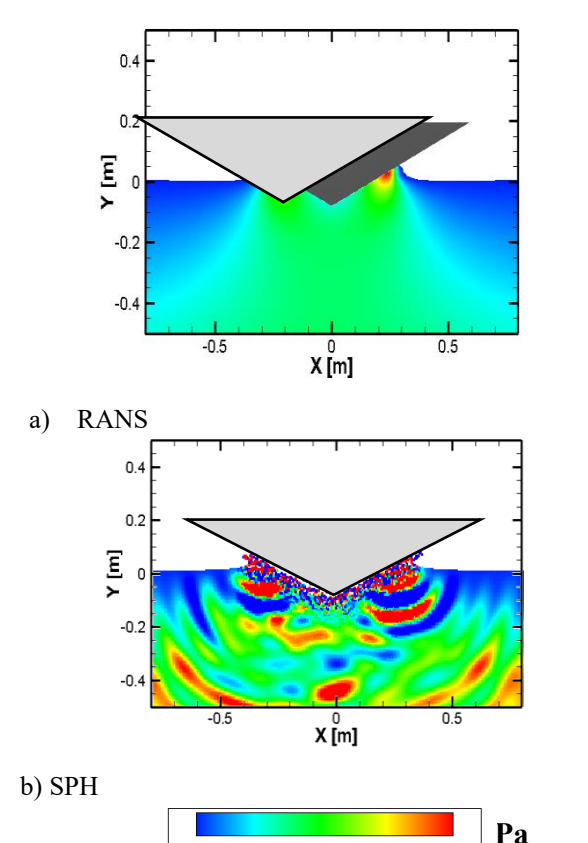
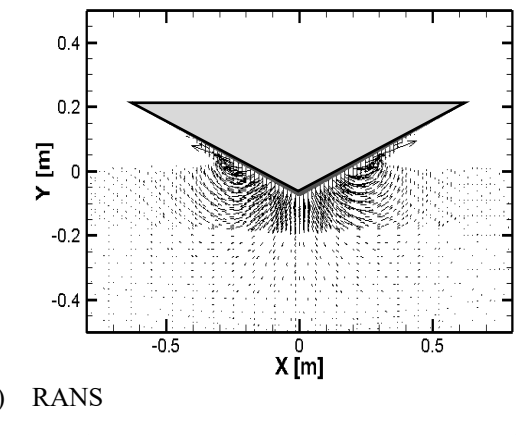


Fig. 15 Distribution of pressure field calculated by RANS model (a); SPH model (b), at t=0.045 s

6000 12000 18000 24000



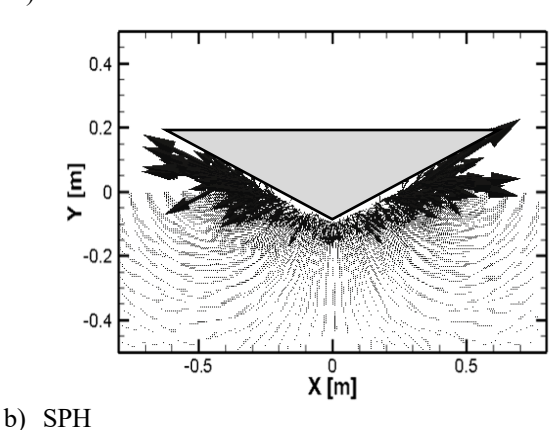


Fig. 16 Numerical speed vector distribution: RANS approach (a); SPH model (b), at t=0.045 s

turbulence modeling, produces smoother fields and more stable pressure predictions, especially for the cylindrical case. These differences affect the representation of cavity dynamics, splash behavior, and velocity gradients near the body and free surface.

4. CONCLUSION

This article investigates the free fall of two rigid bodies—a cylinder and a wedge—into a fluid initially at rest. The study employs two 2D numerical approaches to describe the temporal evolution of speed, displacement, and pressure for these objects: the Reynolds-Averaged Navier-Stokes (RANS) approach and the Smoothed-Particle Hydrodynamics (SPH) method. These two approaches are compared with experimental measurements to evaluate their accuracy and determine which method provides the most reliable predictions for the physical variables involved.

The main objective of this work is to assess the performance of the RANS and SPH models in simulating the interaction between the rigid bodies and the fluid, particularly focusing on displacement, pressure, and velocity. Both models give good predictions of the rigid body displacement when compared to the experimental data. However, while the RANS approach demonstrates a clear advantage in accurately predicting the pressure field, especially in cases of complex fluid behavior like the discontinuity between the fluid and air domains, the SPH model shows limitations. The SPH method, which relies on empirical formulations, struggles with accurately modeling pressure fields under such conditions due to the inherent challenges of particle scattering and boundary reflections.

In terms of speed prediction, both models capture the general trend, but the SPH model tends to deviate as the object approaches the free surface, especially when large displacements occur. The RANS method, in contrast, provides more stable results throughout the simulation, particularly in scenarios involving complex fluid-structure interactions, such as during the break between fluid and air domains.

Future developments in SPH may focus on reducing spurious pressure oscillations through improved pressure stabilization methods (e.g., δ -SPH, ISPH), while adaptive particle refinement and hybrid turbulence models (RANS/LES) can help minimize differences observed in velocity fields, pressure distributions, and streamline patterns. These enhancements would improve the accuracy and robustness of SPH for simulating rigid body impacts with free-surface flows.

Similarly, further enhancements to the RANS approach could involve improving free-surface resolution using advanced VOF interface-capturing schemes and pressure-peak modeling near impact regions. The integration of dynamic mesh techniques and hybrid turbulence models (e.g., RANS/LES) may also help reduce discrepancies observed in the velocity and pressure fields, as well as streamline representation, particularly in highly transient rigid body–fluid interaction scenarios.

This study highlights the strengths and weaknesses of both approaches and demonstrates that while the RANS model is more reliable for pressure predictions and cases involving significant fluid-structure interactions, the SPH method can still provide valuable insights, particularly in cases involving large rigid body displacements. Ultimately, this research provides a solid foundation for the design of floating bodies and guides future efforts to methods for fluid-structure enhance numerical interactions. The findings inform the selection of modeling approaches in applications such as wavestructure interactions, slamming loads on hulls, and coastal impact scenarios. Specifically, RANS methods are preferred for accurate pressure prediction, while SPH demonstrates superior capability in capturing violent freesurface deformations.

Future improvements of both WCSPH and RANS/VOF methods should prioritize extending 2D simulations to fully three-dimensional models, enabling better capture of asymmetric cavity formation, splashing, and lateral flow effects inherent to rigid body water entry. For this rigid body study, 3D modeling offers the most significant enhancement by improving accuracy in flow features underrepresented in 2D. Additionally, incorporating deformable coupling in WCSPH would allow simulation of structural responses relevant to flexible bodies, while RANS/VOF could benefit from advanced interface capturing, turbulence models, and deformable structural coupling to better handle fluidstructure interactions during impacts. These developments would help reduce discrepancies in velocity, pressure, and streamline predictions, enhancing overall reliability.

CONFLICT OF INTEREST

The authors declare that they have no conflict of interest

AUTHORS CONTRIBUTION

Ahmed Bel Hadj Taher: Visualization, Methodology, Software, Formal Analysis, Investigation, Resources, Data Curation, Writing of the Original Draft. Marwa Ennouri: Methodology, Validation, Writing of the Final Manuscript, Review and Editing. Hatem Kanfoudi: Validation, Supervision, Methodology, Review and Editing.

REFERENCES

- Altomare, C., Crespo, A. J. C., Domínguez, J. M., Gómez-Gesteira, M., Suzuki, T., & Verwaest, T. (2015). Applicability of Smoothed Particle Hydrodynamics for estimation of sea wave impact on coastal structures. *Coastal Engineering*, 96, 1-12. https://doi.org/10.1016/j.coastaleng.2014.11.001
- Antuono, M., Colagrossi, A., Marrone, S., & Molteni, D. (2010). Free-surface flows solved by means of SPH schemes with numerical diffusive terms. *Computer Physics Communications*, 181(3), 532–549. https://doi.org/10.1016/j.cpc.2009.11.002

- Batchelor, G. K. (2000). *An introduction to fluid dynamics*. Cambridge University Press. https://doi.org/10.1017/CBO9780511800955
- Belytschko, T., Liu, W., Moran, B., & Elkhodary, K. (2014). *Nonlinear finite elements for continua and structures* (2nd ed.). John Wiley & Sons.
- Brizzolara, S., Savio, L., Viviani, M., Chen, Y., Temarel,
 P., Couty, N., Hoflack, S., Diebold, L., Moirod, N.,
 & Souto Iglesias, A. (2009). Comparison of experimental and numerical sloshing loads in partially filled tanks. *Analysis and Design of Marine Structures*, 13–26.
- Campbell, I. M. C., & Weynberg, P. A. (1980).

 Measurement of parameters affecting slamming
 (Rapport technique No. 440). Wolfson Unit for
 Marine Technology, Université de Southampton
- Chang, K.-A., Hsu, T.-J., & Liu, P. L.-F. (2001). Vortex generation and evolution in water waves propagating over a submerged rectangular obstacle: Part I. Solitary waves. *Coastal Engineering*, 44, 13–36. https://doi.org/10.1016/S0378-3839(01)00044-7
- Chang, K.-A., Hsu, T.-J., & Liu, P. L.-F. (2005). Vortex generation and evolution in water waves propagating over a submerged rectangular obstacle. Part II: Cnoidal waves. *Coastal Engineering*, *52*(3), 257–283.
 - https://doi.org/10.1016/j.coastaleng.2004.11.006
- Chen, J. X., & Da Vitoria Lobo, N. (1995). Toward interactive-rate simulation of fluids with moving obstacles using Navier-Stokes equations. *Graphical Models and Image Processing*, *57*(2), 107–116. https://doi.org/10.1006/gmip.1995.1012
- Crespo, A. J. C., Dominguez, J. M., Barreiro, A., Gómez-Gesteira, M., & Rogers, B. D. (2011). GPUs, a new tool of acceleration in CFD: Efficiency and reliability on smoothed particle hydrodynamics methods. *PLoS ONE*, 6(6). https://doi.org/10.1371/journal.pone.0020685
- Crespo, A. J. C., Dominguez, J. M., Rogers, B. D., Gómez-Gesteira, M., Longshaw, S., Canelas, R., Vacondio, R., Barreiro, A., & García-Feal, O. (2015). DualSPHysics: Open-source parallel CFD solver based on Smoothed Particle Hydrodynamics (SPH). Computer Physics Communications, 187, 204–216. https://doi.org/10.1016/j.cpc.2014.10.004
- Crespo, A. J. C., Gómez-Gesteira, M., & Dalrymple, R. A. (2008). Modeling dam break behavior over a wet bed by a SPH technique. *Journal of Waterway, Port, Coastal, and Ocean Engineering, 134*(6), 313–320. https://doi.org/10.1061/asce0733-950x2008134:6313
- Cundall, P. A., & Strack, O. D. L. (1979). A discrete numerical model for granular assemblies. *Géotechnique*, 29(1), 47–65. https://doi.org/10.1680/geot.1979.29.1.47
- Dalrymple, R. A., & Rogers, B. D. (2006). Numerical modeling of water waves with the SPH method.

- *Coastal Engineering*, *53*(2–3), 141–147. https://doi.org/10.1016/j.coastaleng.2005.10.004
- Dominguez, J. M., Fourtakas, G., Altomare, C., Canelas, R. B., Tafuni, A., García-Feal, O., Martínez-Estévez, I., Mokos, A., Vacondio, R., Crespo, A. J. C., Rogers, B. D., Stansby, P. K., & Gómez-Gesteira, M. (2022). DualSPHysics: from fluid dynamics to multiphysics problems. *Computational Particle Mechanics*, 9(5), 867–895. https://doi.org/10.1007/s40571-021-00404-2
- Faltinsen, O. M., Kjerland, O. K., Tørum, N. A., & Nguyen, T. V. (1977). Water impact loads and dynamic response of horizontal circular cylinders in offshore structures. *Proceedings of the Offshore Technology*Conference. https://doi.org/10.4043/2741-MS
- Fang, J., Parriaux, A., Rentschler, M., & Ancey, C. (2009). Improved SPH methods for simulating free surface flows of viscous fluids. *Applied Numerical Mathematics*, 59(2), 251–271. https://doi.org/10.1016/j.apnum.2008.02.003
- Gingold, R. A., & Monaghan, J. J. (1977). Smoothed particle hydrodynamics: theory and application to non-spherical stars. *Monthly Notices of the Royal Astronomical Society*, 181(3), 375–389. https://doi.org/10.1093/mnras/181.3.375
- Gomez-Gesteira, M. (2010). State-of-the-art of classical SPH for free-surface flows. *Journal of Hydraulic Research*, 48(extra), 6–27. https://doi.org/10.3826/jhr.2010.0012
- Gomez-Gesteira, M., Dalrymple, R. A., & Asce, F. (2004). Using a three-dimensional smoothed particle hydrodynamics method for wave impact on a tall structure. *Journal of Waterway, Port, Coastal and Ocean Engineering, 130*(2), 63–69. https://doi.org/10.1061/asce0733-950x2004130:263
- Greenhow, M., & Lin, W.-M. (1983). Nonlinear free surface effects: Experiments and theory. *MIT Department of Ocean Engineering Report No. 83-19*.
- Hagiwara, K., & Yuhara, T. (1975). Fundamental Study of Wave Impact Loads on Ship Bow (3rd Report). Journal of the Society of Naval Architects of Japan, (137), 240–245. https://doi.org/10.2534/jjasnaoe1968.1975.240
- Hirt, C. W., Amsden, A. A., & Cook, J. L. (1974). An arbitrary Lagrangian-Eulerian computing method for all flow speeds. *Journal of Computational Physics*, 135, 203–216. https://doi.org/https://doi.org/10.1016/0021-9991(74)90051-5
- Hosain, M. L., Sand, U., & Fdhila, R. B. (2018). Numerical Investigation of Liquid Sloshing in Carrier Ship Fuel Tanks. *IFAC-PapersOnLine*, 51(2), 583–588. https://doi.org/10.1016/J.IFACOL.2018.03.098
- Johnson, G. R., Stryk, R. A., & Beissel, S. R. (1996). SPH for high velocity impact computations. *Computer*

- Methods in Applied Mechanics and Engineering, 139(1–4), 347–373. https://doi.org/10.1016/S0045-7825(96)01089-4
- Lal, A., & Elangovan, M. (2008). CFD Simulation and Validation of Flap Type Wave-Maker. International *Journal of Engineering, Mathematical and Physical Sciences*, 2, 10, 708–7014.
- Landau, L. D., & Lifshitz, E. M. (2014). *Fluid mechanics* (Vol. 6). Elsevier Science.
- Liu, P. L. F., & Al-Banaa, K. (2004). Solitary wave runup and force on a vertical barrier. *Journal of Fluid Mechanics*, 505, 225–233. https://doi.org/10.1017/S0022112004008547
- Losasso, F., Talton, J. O., Kwatra, N., & Fedkiw, R. (2008). Two-way coupled SPH and particle level set fluid simulation. *IEEE Transactions on Visualization and Computer Graphics*, 14(4), 797–804. https://doi.org/10.1109/tvcg.2008.37
- Lucy, L. B. (1977). A numerical approach to the testing of the fission hypothesis. *The Astronomical Journal*, 82, 1013–1024. https://doi.org/10.1086/112164
- Mahmoodi, M., Shademani, R., & Gorji Bandpy, M. (2018). Viscous Models Comparison in Water Impact of Twin 2D Falling Wedges Simulation by Different Numerical Solvers. *International Journal of Maritime Technology*, 9(1), 1–13. https://doi.org/10.29252/ijmt.9.1
- Monaghan, J. J. (1994). Simulating Free Surface Flows with SPH. *Journal of Computational Physics*, 110(2), 399–406. https://doi.org/10.1006/jcph.1994.1034
- Morris, J. P. (1996). A Study of the Stability Properties of Smooth Particle Hydrodynamics. *Publications of the Astronomical Society of Australia*, *13*(1), 97–102. https://doi.org/10.1017/S1323358000020610
- Müller, M., Charypar, D., & Gross, M. (2003). Particle-based fluid simulation for interactive applications. Proceedings of the 2003 ACM SIGGRAPH/Eurographics Symposium on Computer Animation, 154–159. San Diego, CA, USA, July 26–27.
- Neves, D. R. C. B., Pires-Silva, A. A., Fortes, C. J. E. M., & Matos, J. J. G. (2016). Comparison of Wave Breaking with RANS and SPH numerical models. Proceedings of the Twenty-Sixth (2016) International Ocean and Polar Engineering Conference.
- O'Brien, J. F., Zordan, V. B., & Hodgins, J. K. (2000). Combining Active and Passive Simulations for Secondary Motion. *IEEE Computer Graphics and Applications*, 20(4), 86–96. https://doi.org/10.1109/38.851756
- Panizzo, A. (2004a). *Physical and numerical modelling of subaerial landslide generated waves* (Doctoral dissertation, University of L'Aquila).

- Panizzo, A. (2004b). SPH modelling of water waves generated by landslides. In *Proceedings of the Convegno di Idraulica e Costruzioni Idrauliche IDRA*.
- Panizzo, A., & Dalrymple, R. A. (2004). SPH modelling of underwater landslide generated waves. *International Conference Coastal Engineering*.
- Rogers, B. D., Dalrymple, R. A., & Stansby, P. K. (2010). Simulation of caisson breakwater movement using 2-D SPH. *Journal of Hydraulic Research*, 48(Suppl. 1), 135–141. https://doi.org/10.1080/00221686.2010.9641254
- Sasson, M., Chai, S., Beck, G., Jin, Y., & Rafieshahraki, J. (2016). A comparison between Smoothed-Particle Hydrodynamics and RANS Volume of Fluid method in modelling slamming. *Journal of Ocean Engineering and Science*, *1*(2), 119–128. https://doi.org/10.1016/J.JOES.2016.03.004
- Singh, J., & Pal, A. (2023). Numerical Investigation of Water Entry of Hydrophobic Spheres. https://doi.org/https://doi.org/10.48550/arXiv.2306.15289
- Singh, P., Hesla, T. I., & Joseph, D. D. (2003). Distributed Lagrange multiplier method for particulate flows with collisions. *International Journal of Multiphase Flow*, 29(3), 495–509. https://doi.org/10.1016/S0301-9322(02)00164-7
- Tafuni, A., De Giorgi, M. G., & De Rosis, A. (2022). Smoothed Particle Hydrodynamics vs Lattice Boltzmann for the solution of steady and unsteady fluid flows. *Computational Particle Mechanics*, *9*(5), 1049–1071. https://doi.org/10.1007/s40571-021-00447-5

- Takahashi, T., Fujii, H., Kunimatsu, A., Hiwada, K., Saito, T., Tanaka, K., & Ueki, H. (2003). Realistic Animation of Fluid with Splash and Foam. *Computer Graphics Forum*, 22(3), 391–400. https://doi.org/10.1111/1467-8659.00686
- Turhan, E., Ozmen-Cagatay, H., & Tantekin, A. (2019). Modeling flood shock wave propagation with the smoothed particle hydrodynamics (SPH) method: An experimental comparison study. *Applied Ecology and Environmental Research*, 17(2), 3033–3047. https://doi.org/10.15666/aeer/1702 30333047
- Vacondio, R., Rogers, B. D., Stansby, P. K., & Mignosa, P. (2012). A correction for balancing discontinuous bed slopes in two-dimensional smoothed particle hydrodynamics shallow water modeling. *International Journal for Numerical Methods in Fluids*, 71(7), 850–872. https://doi.org/10.1002/fld.3687
- Vacondio, R., Rogers, B. D., Stansby, P. K., & Mignosa, P. (2013). Shallow water SPH for flooding with dynamic particle coalescing and splitting. *Advances in Water Resources*, 58, 10–23. https://doi.org/10.1016/j.advwatres.2013.04.007
- Yettou, E. M., Desrochers, A., & Champoux, Y. (2006). Experimental study on the water impact of a symmetrical wedge. *Fluid Dynamics Research*, 38(1), 47–66. https://doi.org/10.1016/j.fluiddyn.2005.09.003
- Yuk, D., Yim, S. C., & Liu, P. L. F. (2006). Numerical modeling of submarine mass-movement generated waves using RANS model. *Computers and Geosciences*, 32(7), 927–935. https://doi.org/10.1016/j.cageo.2005.10.028